Electronic Supplementary Information

Enantiorecognition in a multi-component environment

Joanna Mazurkiewicz,[a,b] Ewa Stanek,[b,c] Pedro Maximiano,[d] Tiago H. Ferreira,[d] Marta Karpiel,[a,b] Szymon Buda,[a] Justyna Kalinowska-Tłuścik,[a] Pedro N. Simões,[d] Igor Reva,[d] and Agnieszka Kaczor*[a]

[a] J. Mazurkiewicz, M. Karpiel, S. Buda, J. Kalinowska-Tłuścik, Agnieszka Kaczor
Faculty of Chemistry
Jagiellonian University
2 Gronostajowa Str., 30-387 Krakow, Poland
E-mail: agnieszka.kaczor@uj.edu.pl

[b] J. Mazurkiewicz, E Stanek, M. Karpiel
Doctoral School of Exact and Natural Sciences
Jagiellonian University
11 Lojasiewicza Str., 30-348 Krakow, Poland

[c] E. Stanek
Jagiellonian Centre for Experimental Therapeutics (JCET)
Jagiellonian University
14 Bobrzynskiego Str., 30-348 Krakow, Poland

[d] P. Maximiano, T. H. Ferreira, P. N. Simões, I. Reva
CERES, Department of Chemical Engineering
University of Coimbra
R. Sílvio Lima, Coimbra 3030-790, Portugal

Contents

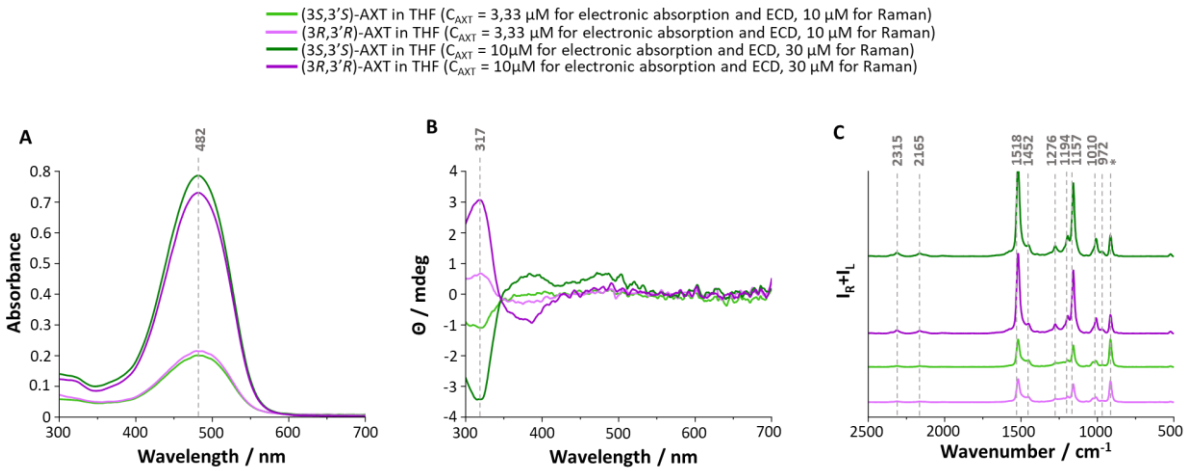

Fig. S1. Electronic absorption, ECD and Raman spectra of AXT dissolved in THF in different concentrations for two enantiomeric forms of AXT – (3S,3'S) and (3*R*,3'*R*). Electronic absorption (**A**) and ECD (**B**) spectra were obtained for molar concentrations of AXT equal to 3.33 µM and 10 µM. Raman spectra (**C**) were obtained for two molar concentrations of AXT equal to 10 µM and 30 µM. Samples for electronic absorption and ECD measurements were diluted threefold in comparison to samples for Raman measurements, to keep absorbance below 1.5.

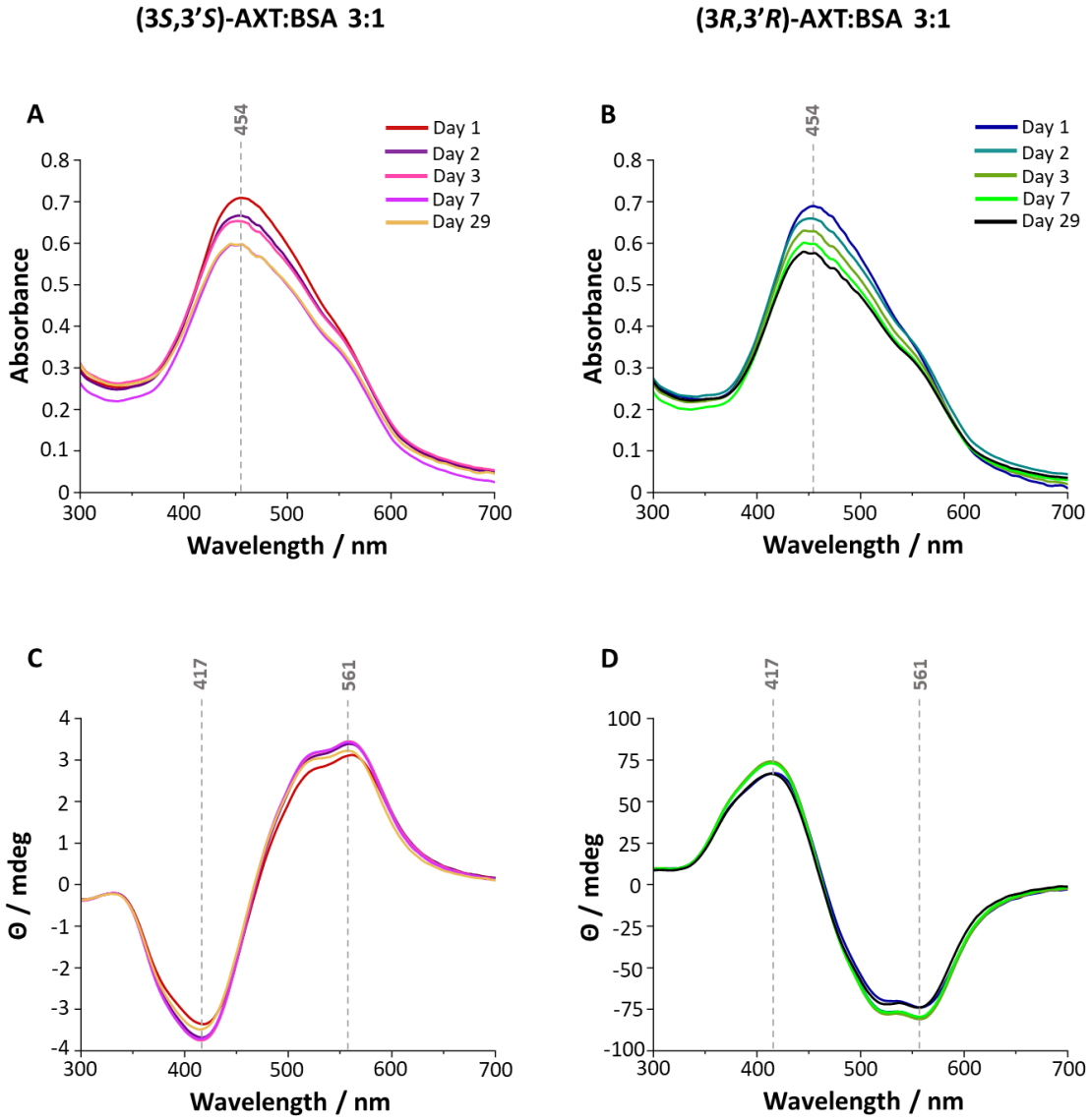

Fig. S2. Room temperature stability of the (3*S*,3'*S*)-AXT:BSA and (3*R*,3'*R*)-AXT:BSA systems monitored by electronic absorption and ECD in the 300-700 nm range. Electronic absorption (**A**,**B**) and ECD (**C**,**D**) spectra of the AXT:BSA complexes with a molar ratio of AXT to BSA equal to 3:1 were measured for 29 days (C_{AXT} = 30 µM, C_{BSA} = 10 µM). A new portion of the sample was measured every time.

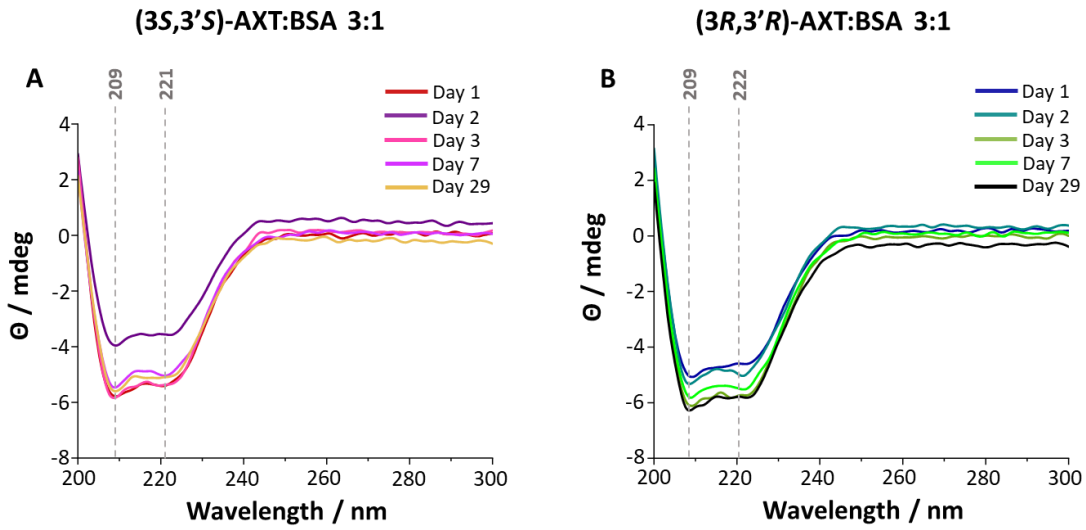

Fig. S3. Room temperature stability of the (3*S*,3'*S*)-AXT:BSA and (3*R*,3'*R*)-AXT:BSA systems monitored by electronic absorption and ECD in the 200-300 nm range. Electronic absorption (**A**) and ECD (**B**) spectra of the AXT:BSA complexes with a molar ratio of AXT to BSA equal to 3:1 were measured for 29 days (C_{AXT} = 1.5 µM, C_{BSA} = 0.5 µM). A new portion of the sample was measured every time.

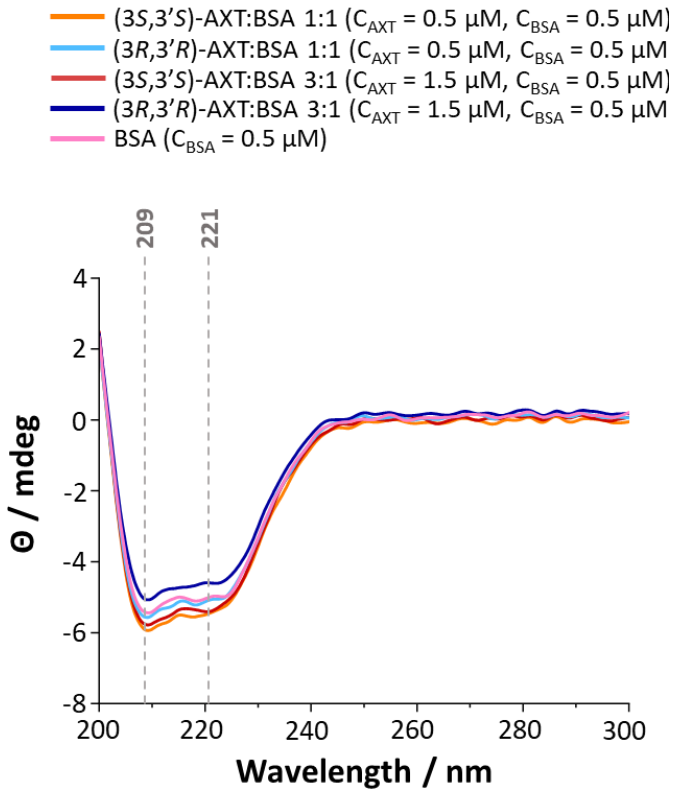

Fig. S4. ECD spectra of AXT:BSA complexes for two enantiomeric forms of AXT – (3*S*,3'*S*) and (3*R*,3'*R*) as well as for BSA dissolved in PBS. The ECD spectra of AXT:BSA complexes were measured for two molar ratios of AXT to BSA equal to 1:1 and 3:1 (C_{AXT} = 0.5 and 1.5= µM; C_{BSA} = 0.5 µM).

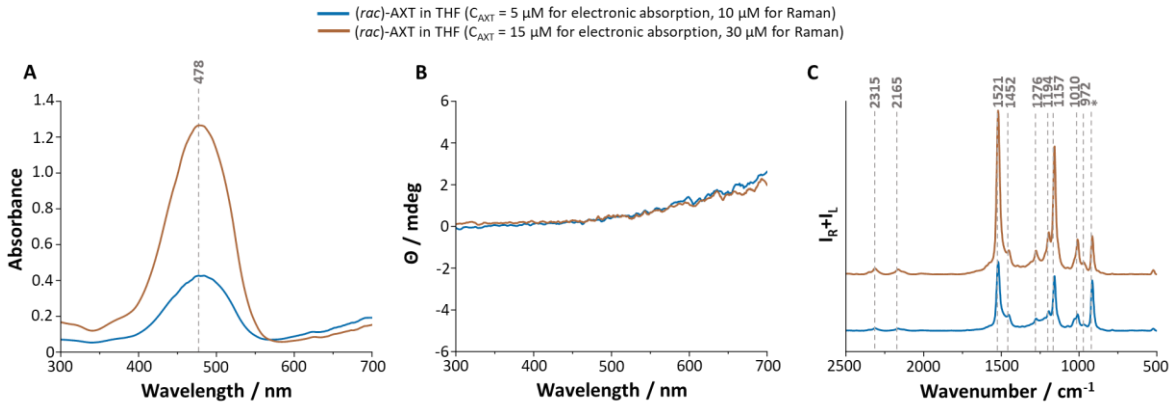

Fig. S5. Electronic absorption, ECD and Raman spectra of (*rac*)-AXT dissolved in THF in different concentrations. Electronic absorption (**A**) and ECD (**B**) spectra were obtained for two molar concentrations of AXT equal to 5 µM and 10 µM. Raman spectra (**C**) were obtained for two molar concentrations of AXT equal to 10 µM and 30 µM. Samples for electronic absorption and ECD measurements were diluted two-fold in comparison to Raman measurements, to keep absorbance below 1.5.* indicates the characteristic band for THF solvent.

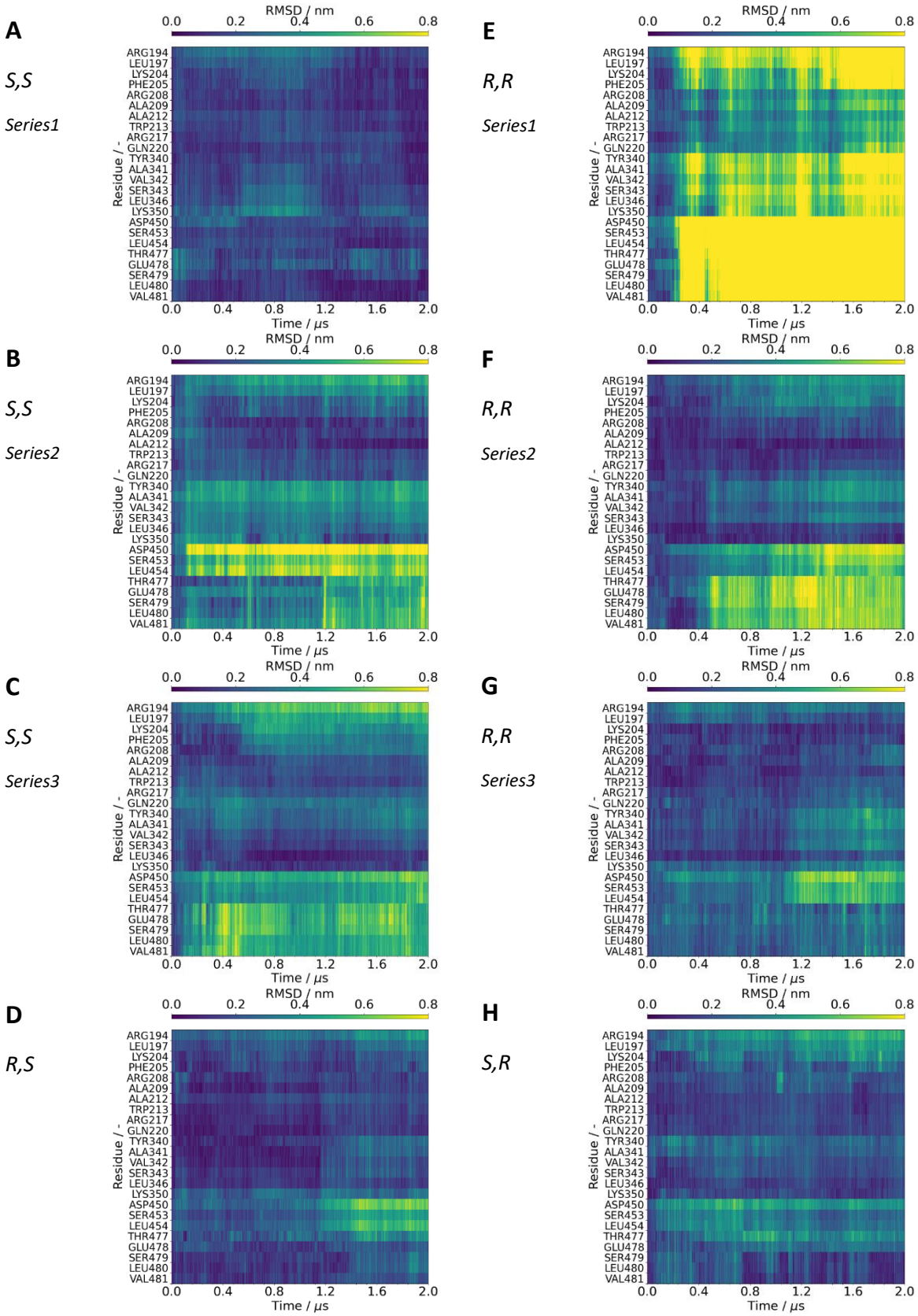

Fig. S6. Root mean square displacement (RMSD) of α-carbon atoms (Cα) of the BSA binding pocket residues for: (**A-C**) (3*S*,3'*S*)-AXT:BSA; (**E-G**) (3*R*,3'*R*)-AXT:BSA; (**D**) (3*R*,3'*S*)-AXT:BSA; (**H**) (3*S*,3'*R*)-AXT:BSA. For (3*S*,3'*S*)-AXT:BSA and (3*R*,3'*R*)-AXT:BSA, the results of three independent runs are shown.

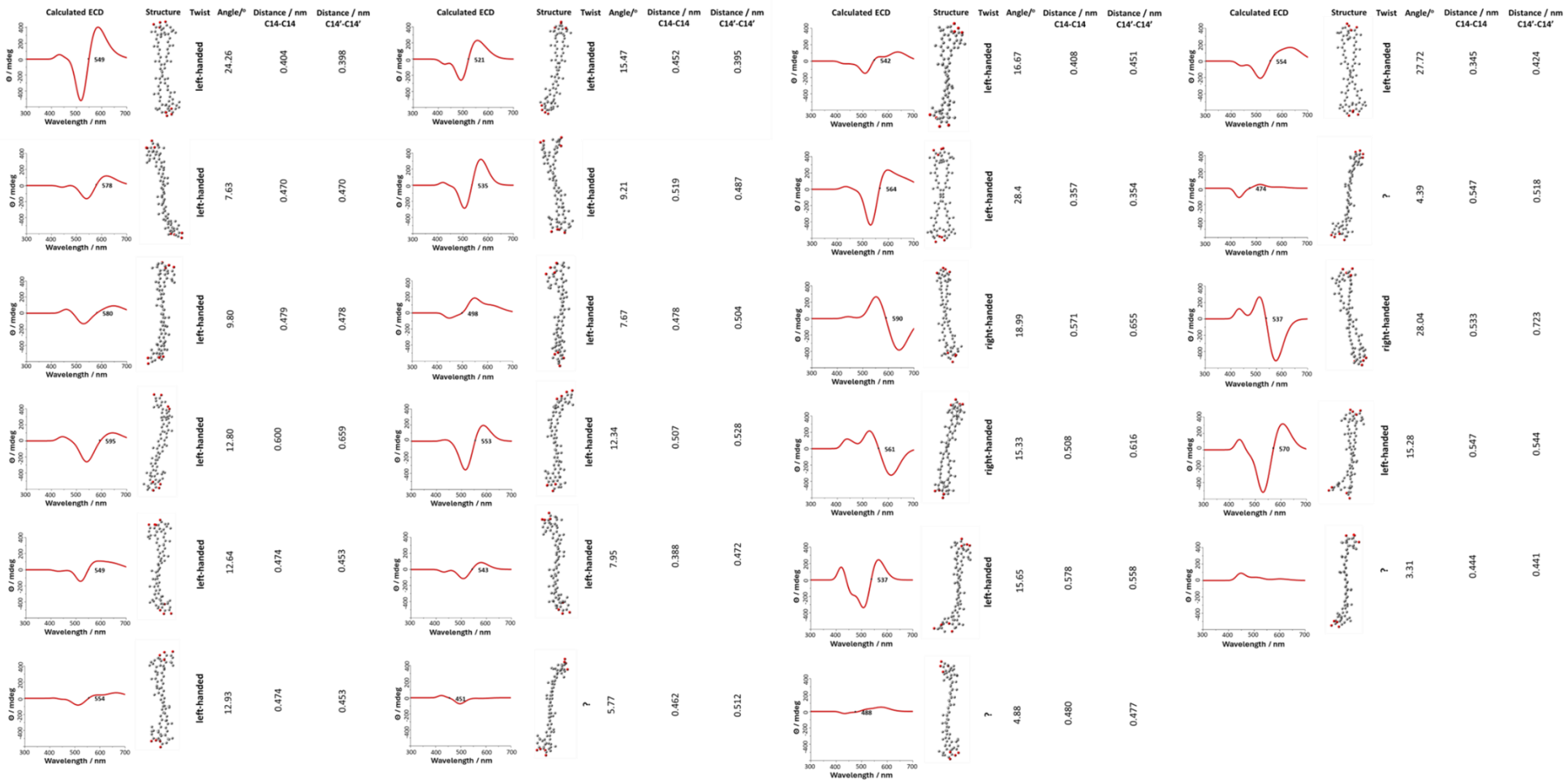

Fig. S7. Calculated ECD spectra of (3*S*,3'*S*)-AXT dimers based on the structures extracted from the molecular dynamics simulation, compared to the structures of the dimers, their helicity, angles and distances between C14-C14 and C14'-C14' pairs of atoms.

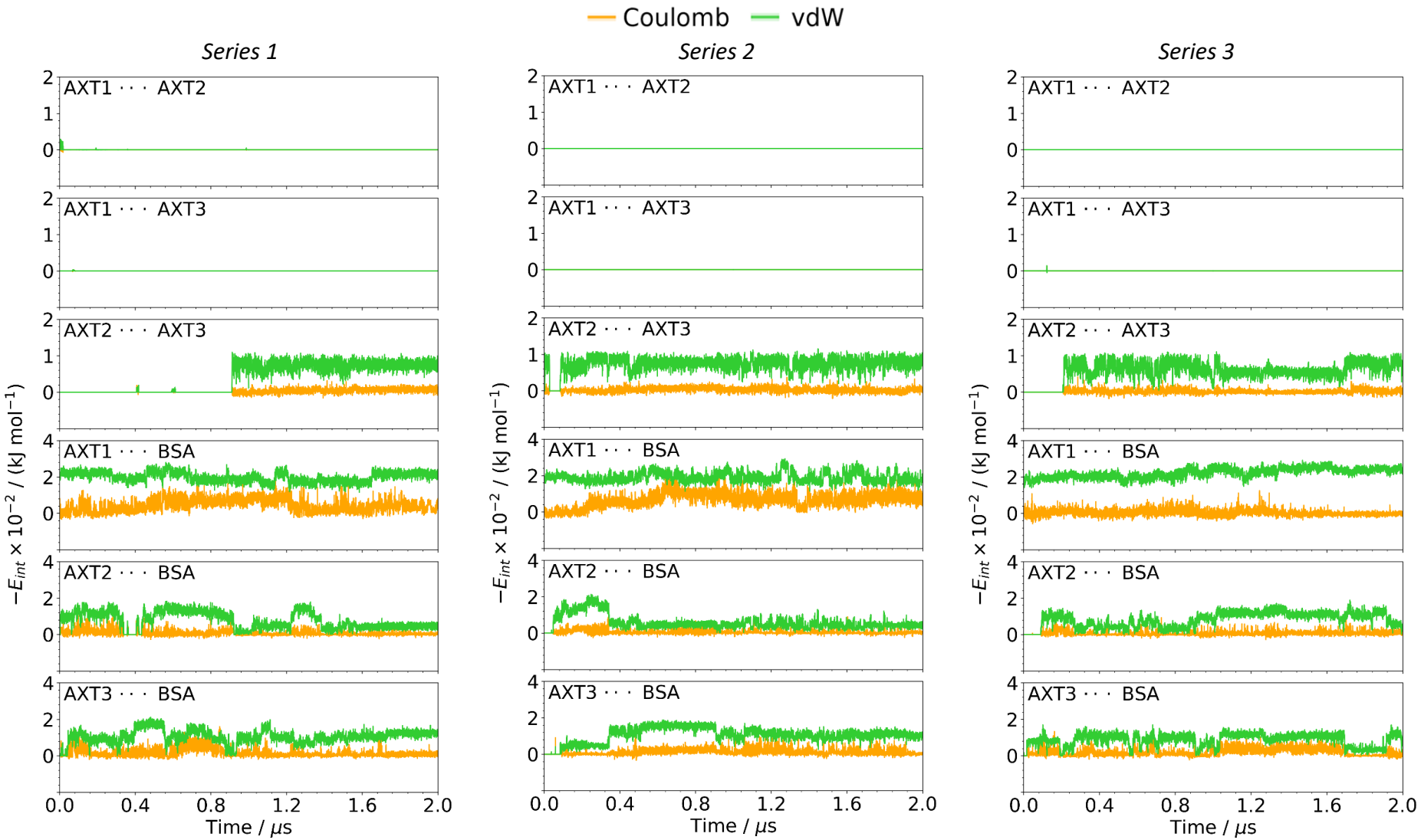

Fig. S8. Coulomb and van der Waals (vdW) interaction energy between AXTi-AXTj and AXTk-BSA for (3*S*,3'*S*)-AXT:BSA systems (results of 3 runs are presented).

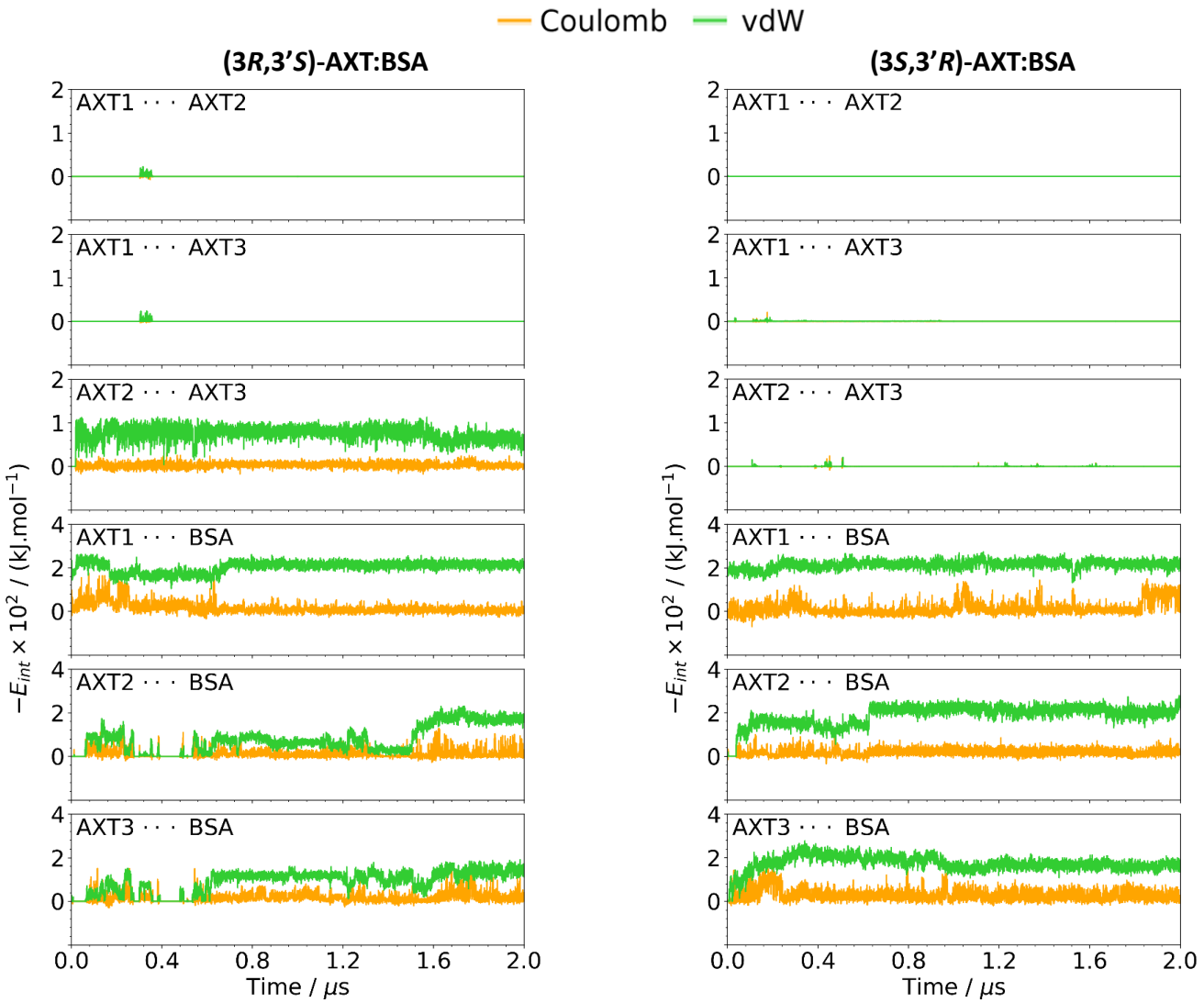

Fig. S9. Coulomb and van der Waals (vdW) interaction energy between AXTi-AXTj and AXTk-BSA for (3*R*,3'*S*)-AXT:BSA and (3*S*,3'*R*)-AXT:BSA systems.

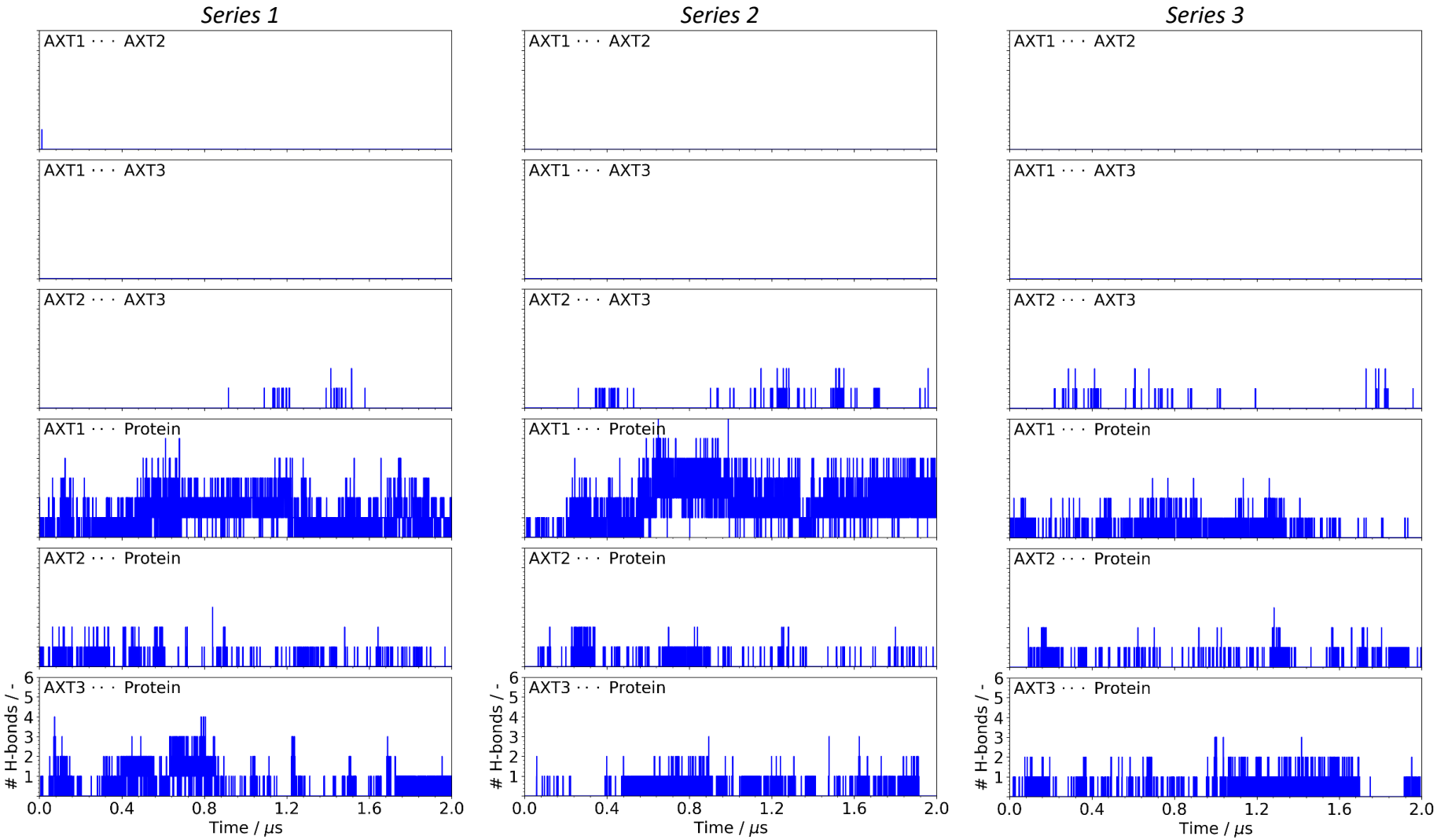

Fig. S10. Number (#) of *H*-bonds between AXT-AXT and AXT-BSA for (3*S*,3'*S*)-AXT:BSA system (results of three independent runs are shown).

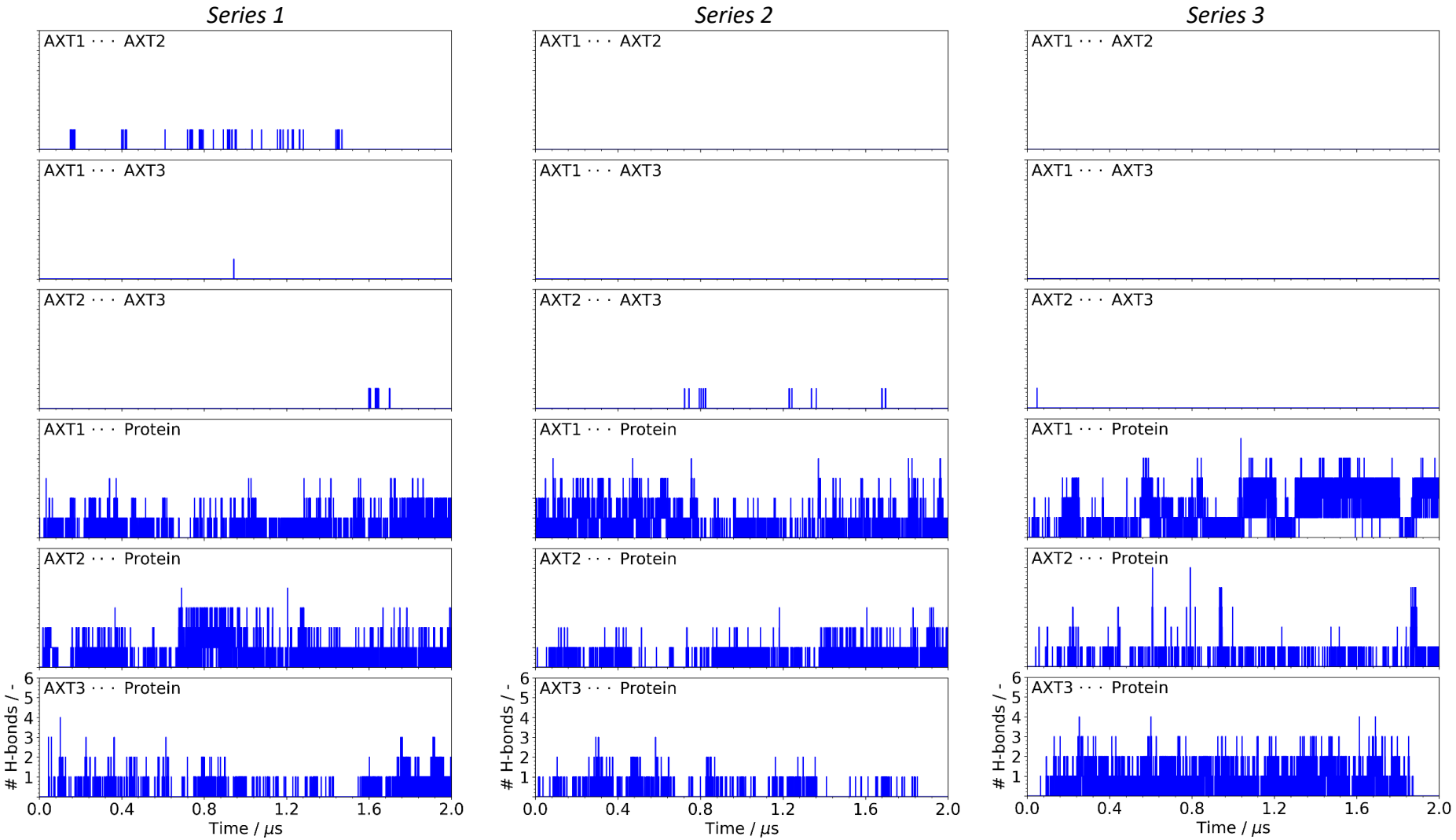

Fig. S11. Number (#) of *H*-bonds between AXT-AXT and AXT-BSA for (3*R*,3'*R*)-AXT:BSA system (results of three independent runs are shown).

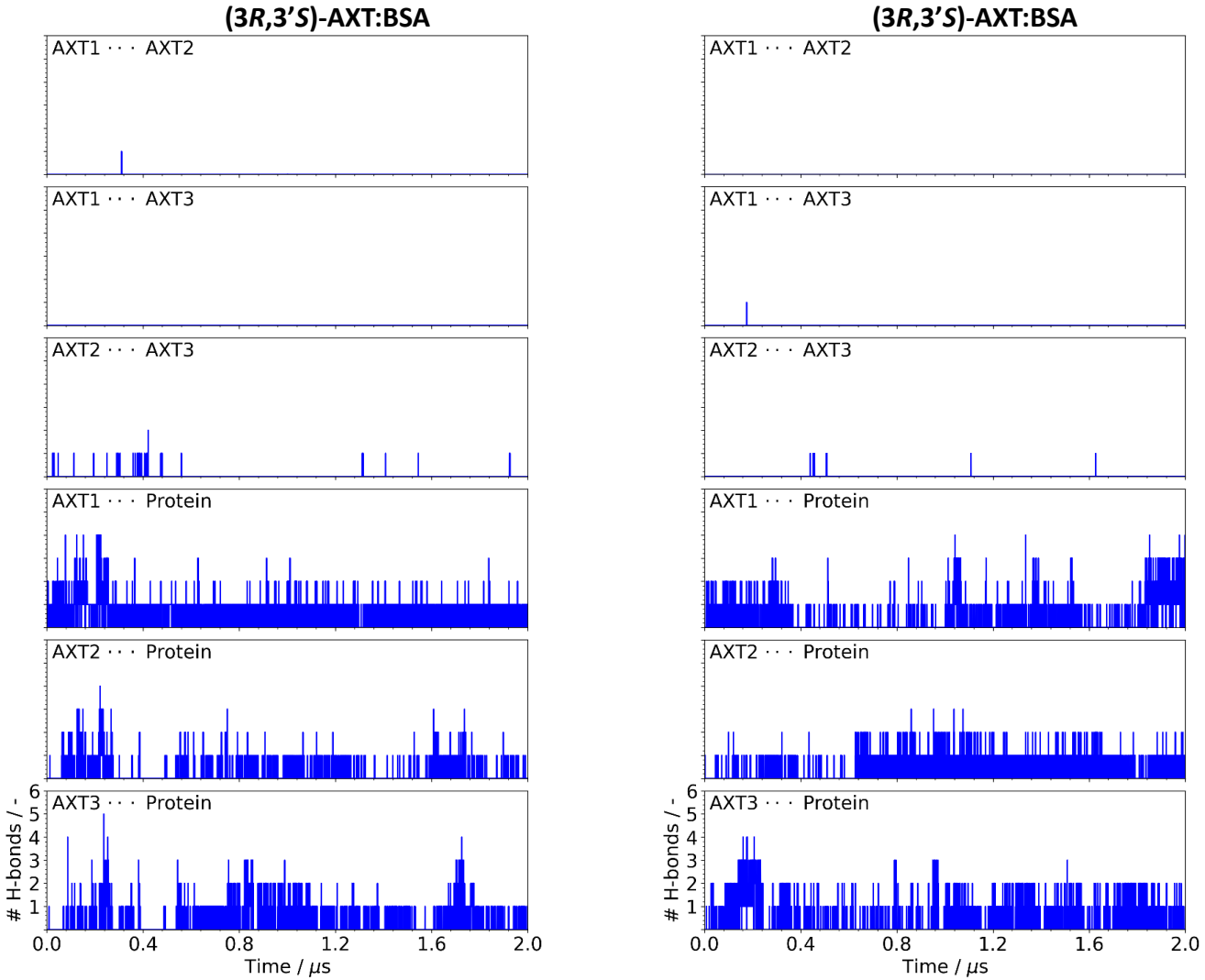

Fig. S12. Number (#) of *H*-bonds between AXT-AXT and AXT-BSA for (3*R*,3'*S*)-AXT:BSA and (3*S*,3'*S*)-AXT:BSA systems.

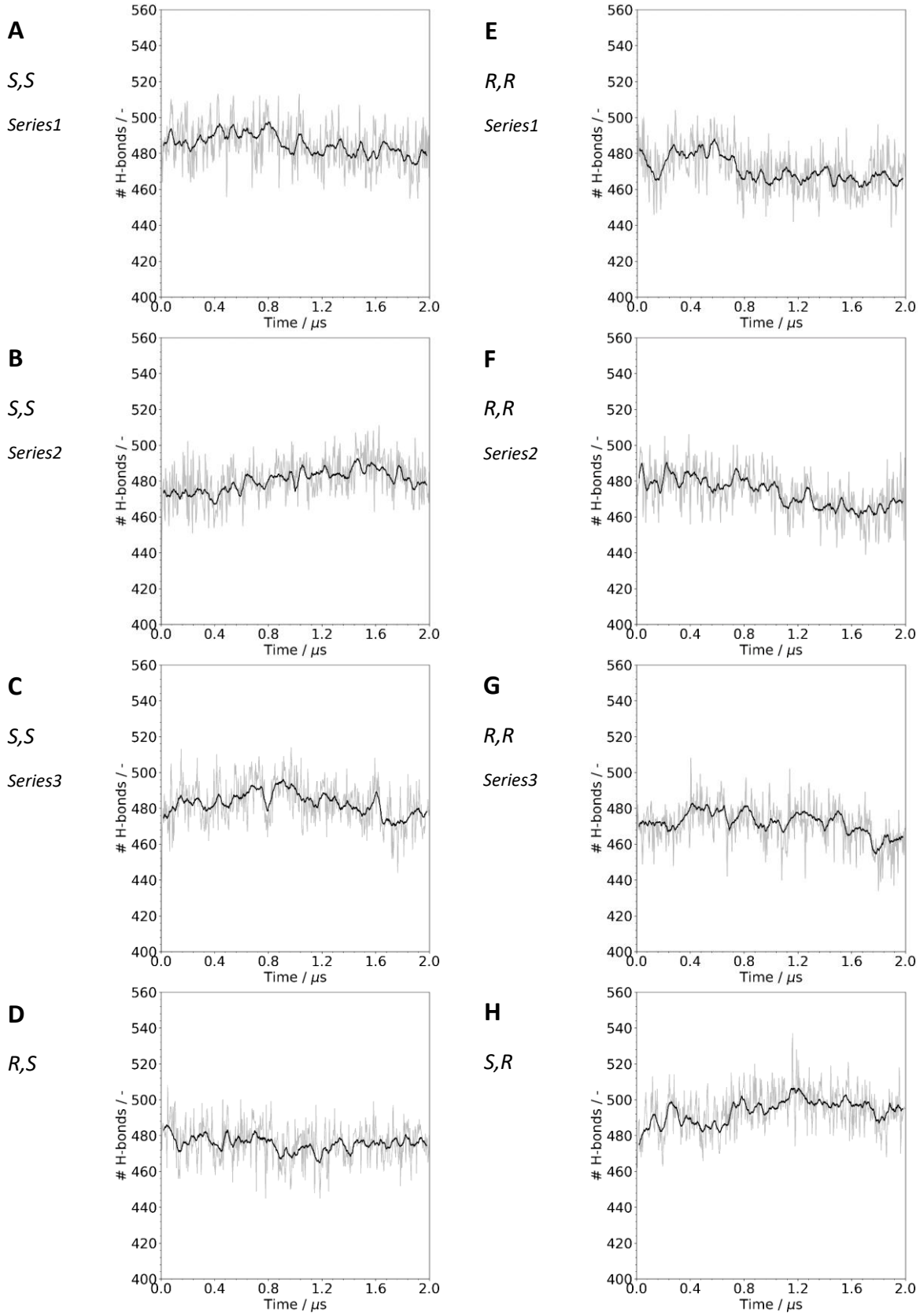

Fig. S13. Number of *H*-bonds in BSA as a function of physical time for: (**A-C**) (3*S*,3'*S*)-AXT:BSA; (**E-G**) (3*R*,3'*R*)-AXT:BSA; (**D**) (3*R*,3'*S*)-AXT:BSA; (**H**) (3*S*,3'*R*)-AXT:BSA. For (3*S*,3'*S*)-AXT:BSA and (3*R*,3'*R*)-AXT:BSA, the results for the three independent runs are shown.

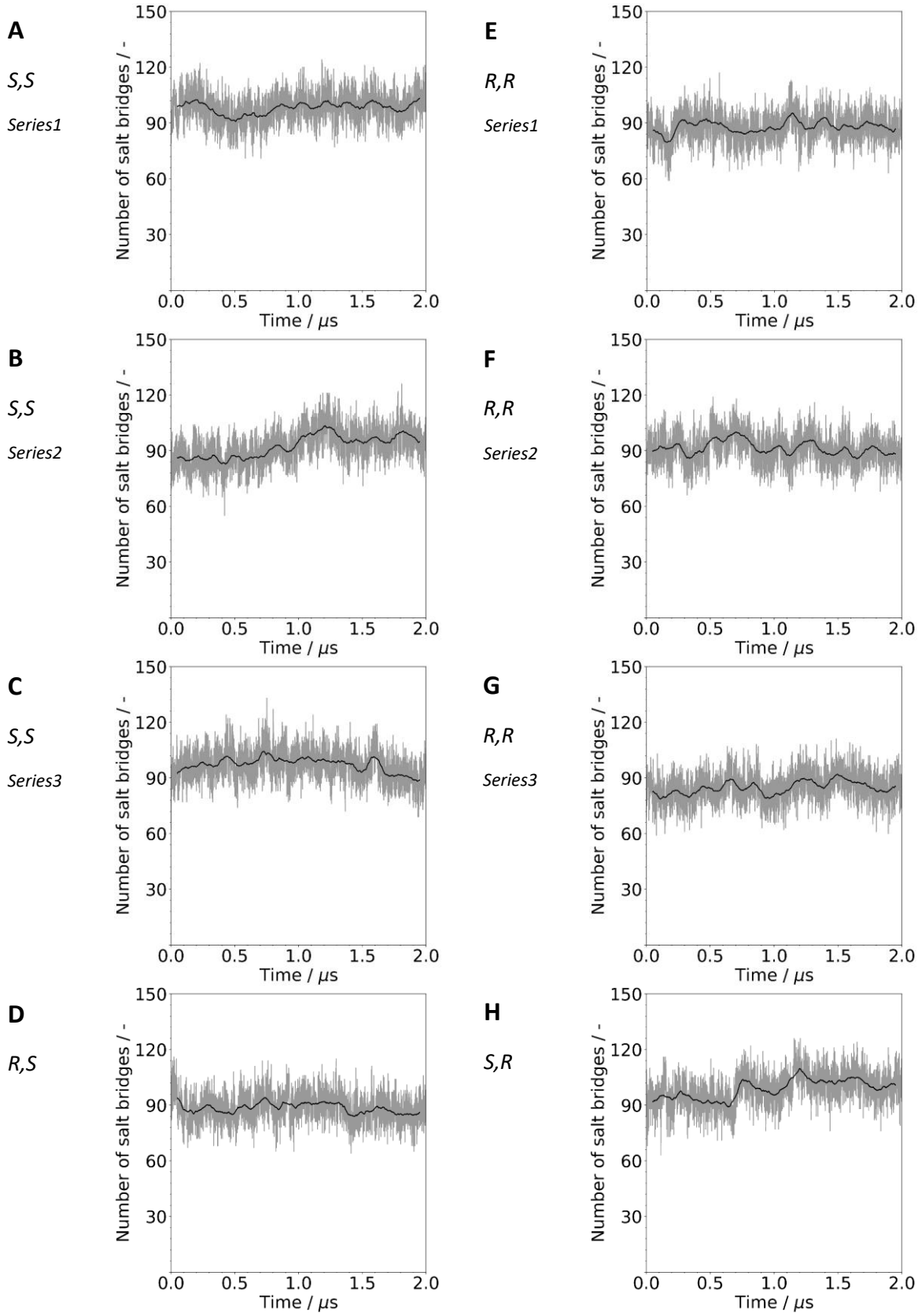

Fig. S14. Number of salt bridges in BSA as a function of physical time for: (**A-C**) (3*S*,3'*S*)-AXT:BSA; (**E-G**) (3*R*,3'*R*)-AXT:BSA; (**D**) (3*R*,3'*S*)-AXT:BSA; (**H**) (3*S*,3'*R*)-AXT:BSA. For (3*S*,3'*S*)-AXT:BSA and (3*R*,3'*R*)-AXT:BSA, the results for the three independent runs are shown.

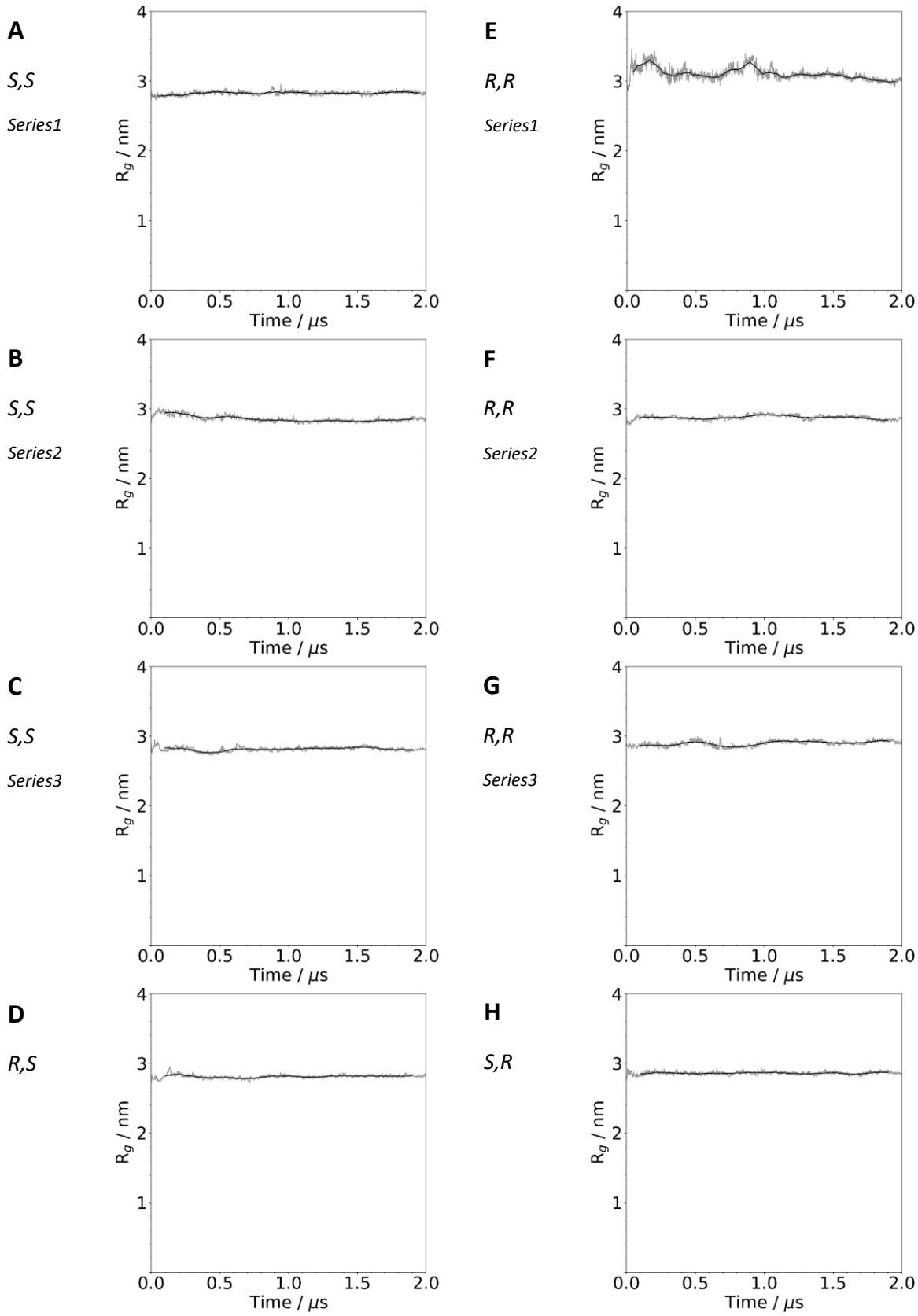

Fig. S15. Radius of gyration of BSA as a function of physical time for: (**A-C**) (3*S*,3'*S*)-AXT:BSA; (**E-G**) (3*R*,3'*R*)-AXT:BSA; (**D**) (3*R*,3'*S*)-AXT:BSA; (**H**) (3*S*,3'*R*)-AXT:BSA. For (3*S*,3'*S*)-AXT:BSA and (3*R*,3'*R*)-AXT:BSA, the results for the three independent runs are shown.

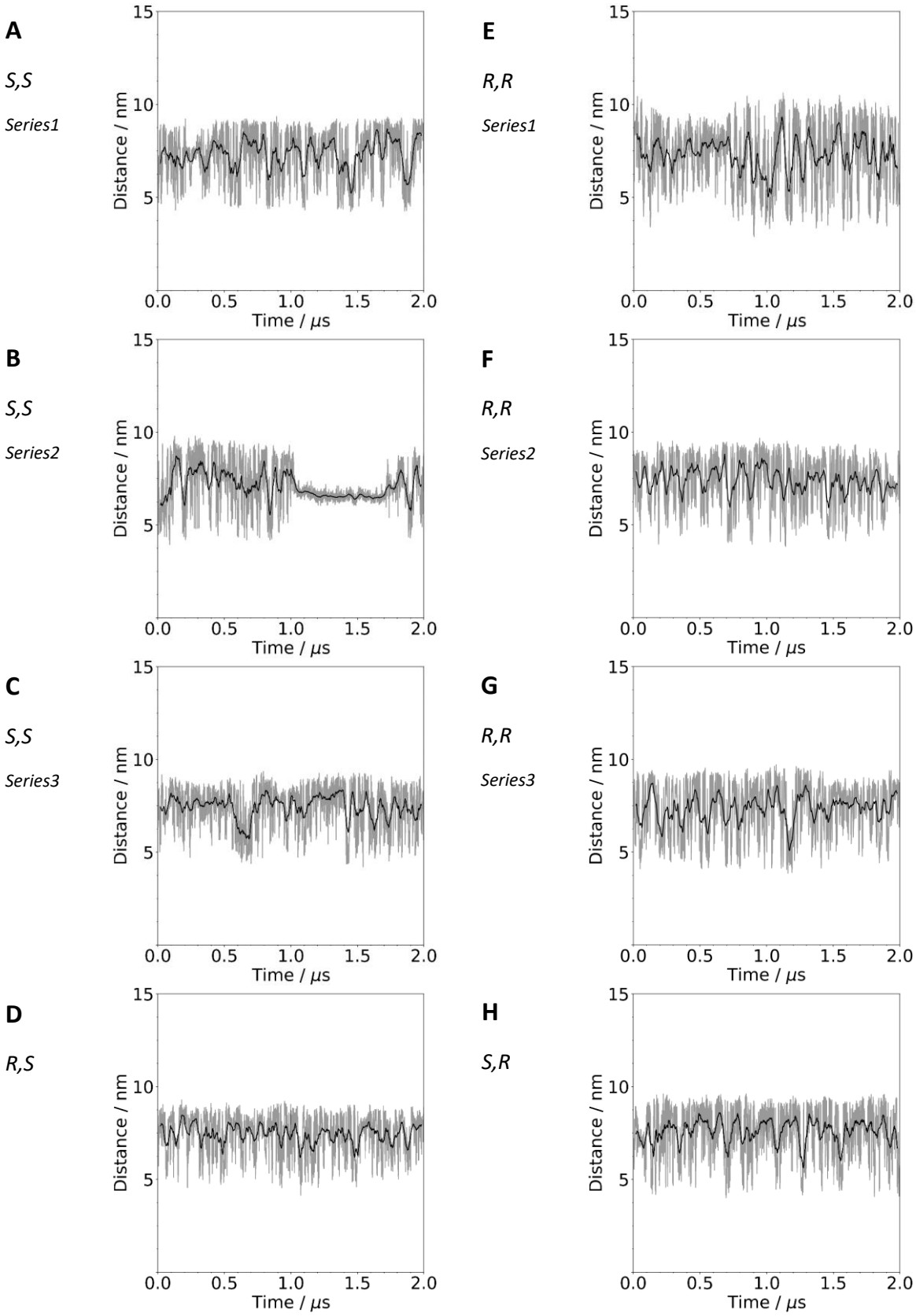

Fig. S16. Head-to-tail distance of BSA as a function of physical time for: (**A-C**) (3*S*,3'*S*)-AXT:BSA; (**E-G**) (3*R*,3'*R*)-AXT:BSA; (**D**) (3*R*,3'*S*)-AXT:BSA; (**H**) (3*S*,3'*R*)-AXT:BSA. For (3*S*,3'*S*)-AXT:BSA and (3*R*,3'*R*)-AXT:BSA, the results for the three independent runs are shown.

Series 1

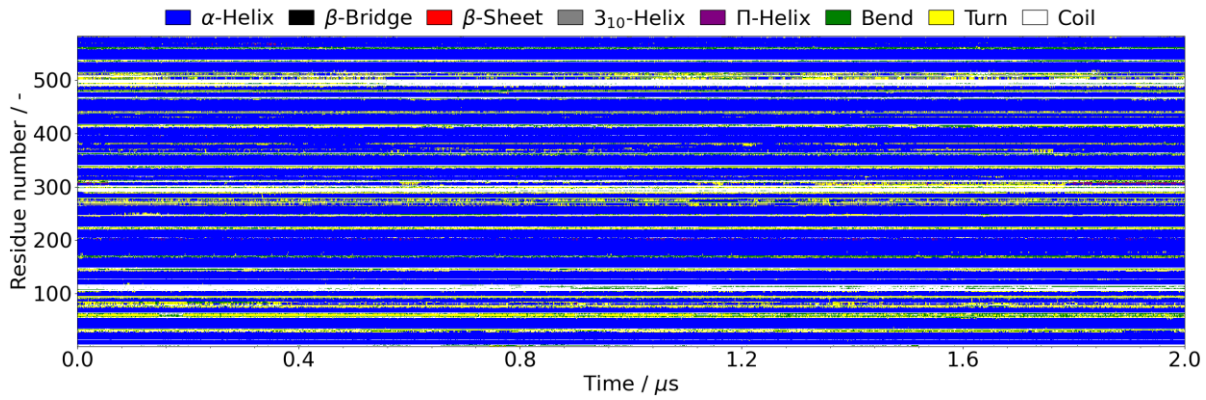

Series 2

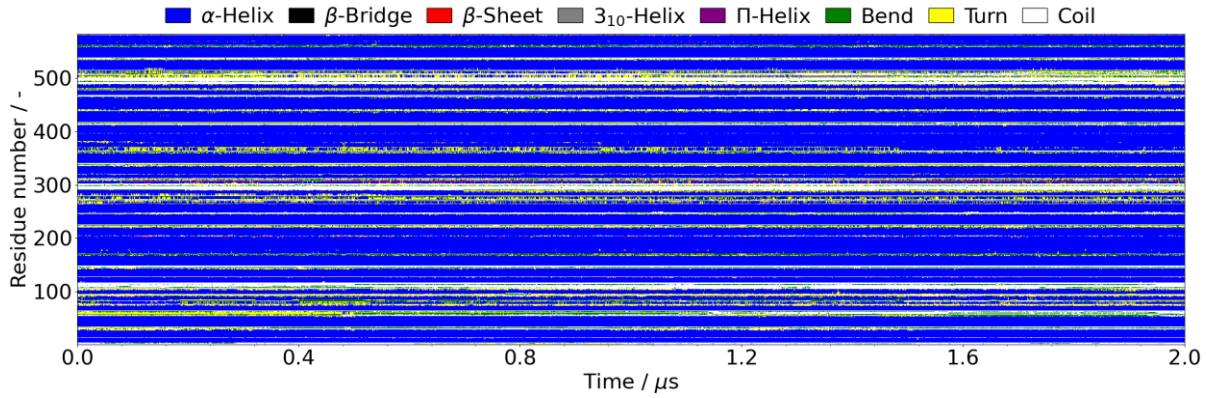

Series 3

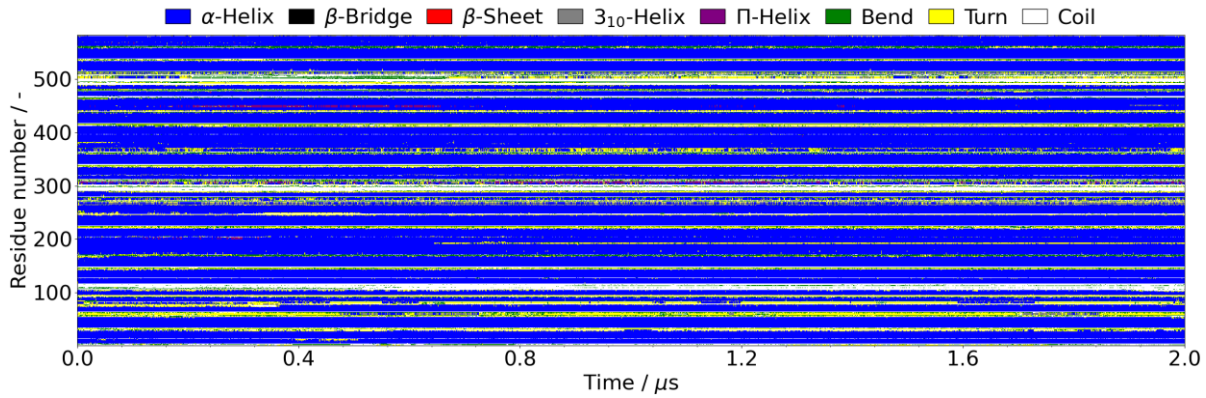

Fig. S17. Secondary structure of the BSA residues as a function of physical time for (3*S*,3'*S*)-AXT:BSA system (results of three independent runs are shown).

Series 1

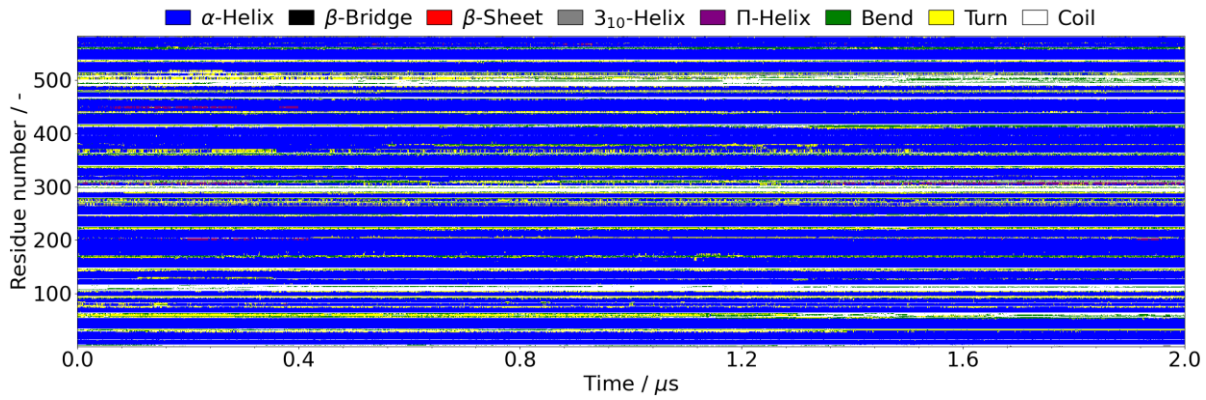

Series 2

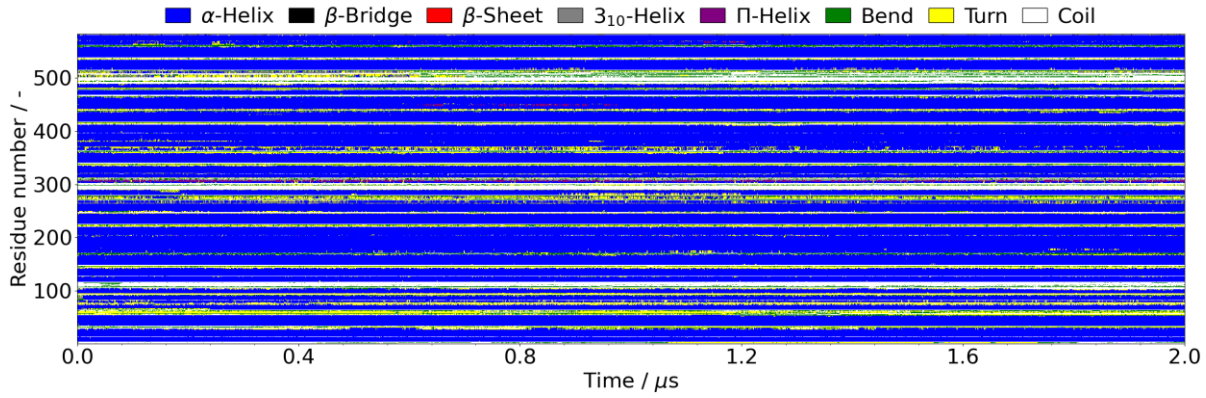

Series 3

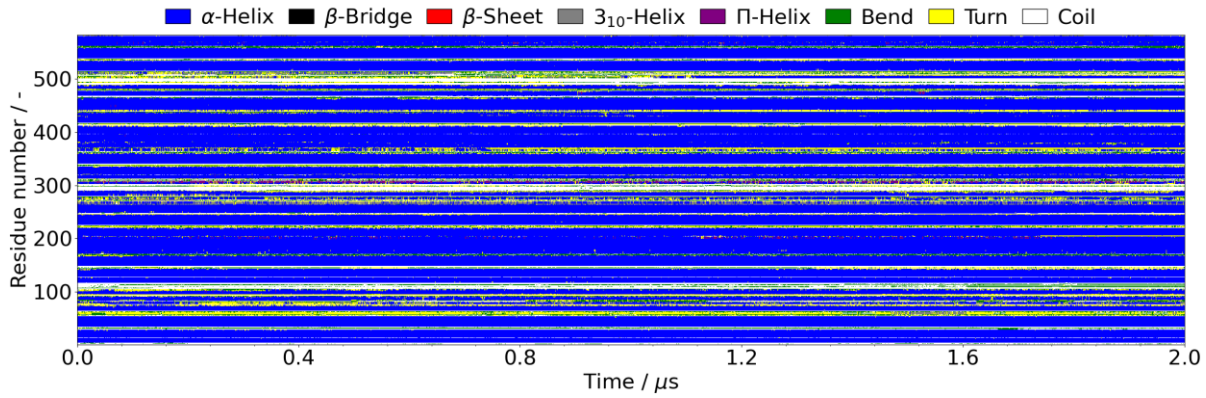

Fig. S18. Secondary structure of the BSA residues as a function of physical time for (3*R*,3'*R*)-AXT:BSA system (results of three independent runs are shown).

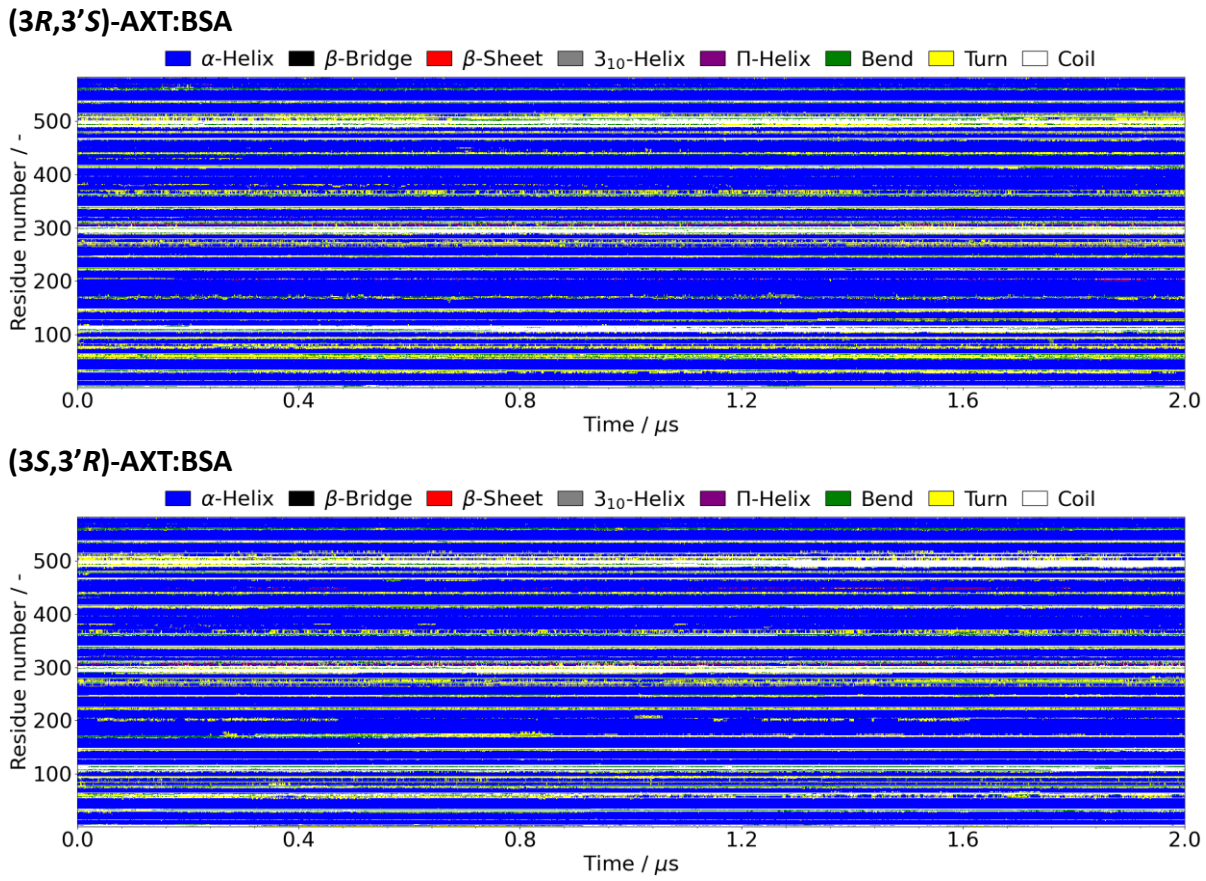

Fig. S19. Secondary structure of the BSA residues as a function of physical time for (3*R*,3'*S*)-AXT:BSA and (3*S*,3'*R*)-AXT:BSA systems.

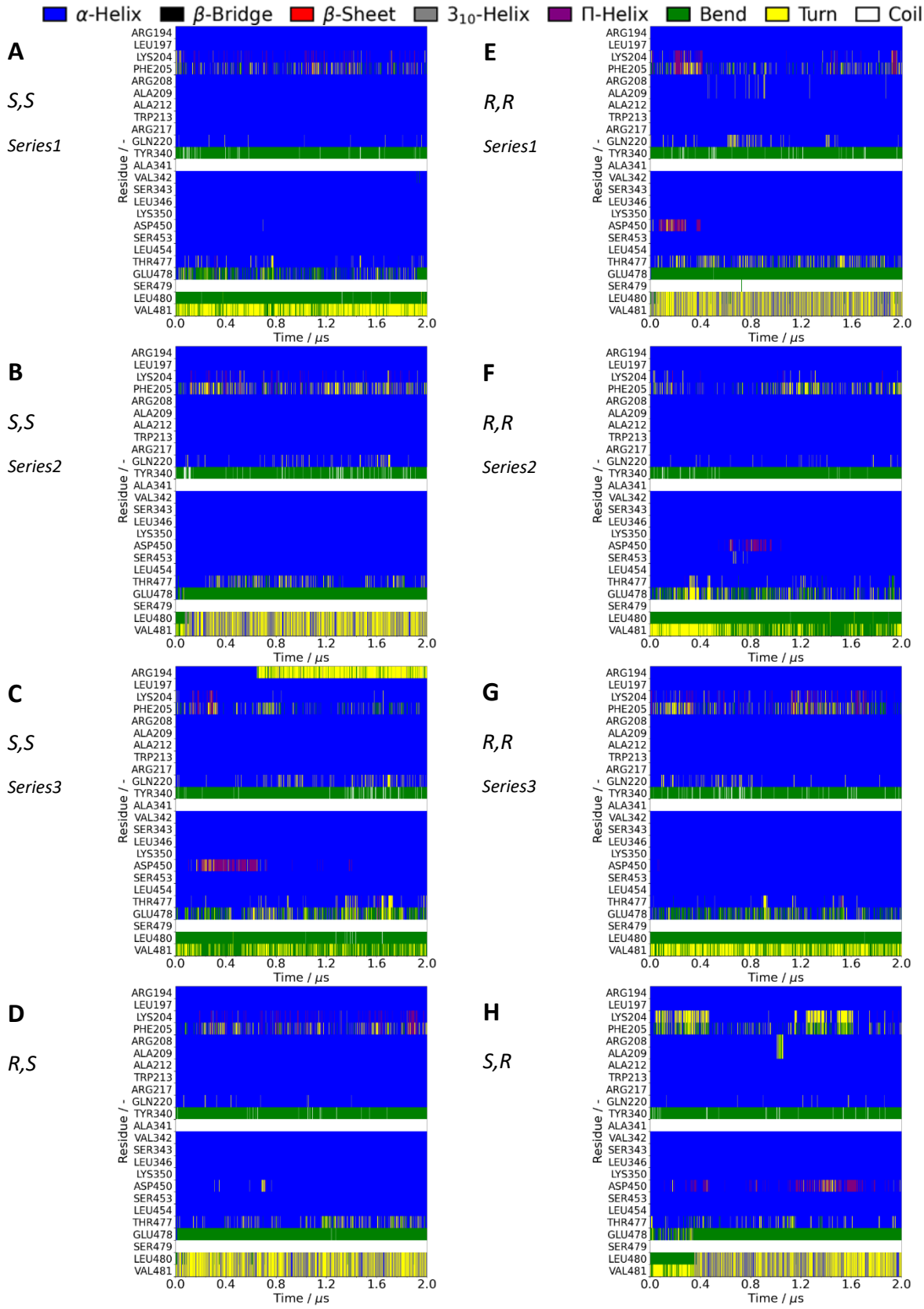

Fig. S20. Secondary structure of the binding pocket residues of the BSA for: (**A-C**) (3*S*,3'*S*)-AXT:BSA; (**E-G**) (3*R*,3'*R*)-AXT:BSA; (**D**) (3*R*,3'*S*)-AXT:BSA; (**H**) (3*S*,3'*R*)-AXT:BSA. For (3*S*,3'*S*)-AXT:BSA and (3*R*,3'*R*)-AXT:BSA, the results of three independent runs are shown.

Table S1. Ratio of integral intensity of 1520 and 1160 cm^{-1} bands in resonance Raman (RR) and RROA spectra for (3*S*,3'*S*)-AXT:BSA and (3*R*,3'*R*)-AXT:BSA complexes with molar ratio of AXT to BSA equal to 1:1 and 3:1.

	Ratio of integral intensity of bands for **(3S,3'S)-AXT**		Ratio of integral intensity of bands for **(3R,3'R)-AXT**	
	$I_{RR\ 3:1}/I_{RR\ 1:1}$	$I_{RROA\ 3:1}/I_{RROA\ 1:1}$	$I_{RR\ 3:1}/I_{RR\ 1:1}$	$I_{RROA\ 3:1}/I_{RROA\ 1:1}$
1520 cm^{-1}	2.532	9.009	2.457	7.813
1160 cm^{-1}	2.451	9.524	2.439	7.634

Table S2. The Chemscore docking results for (3*R*,3'*R*)-AXT, (3*S*,3'*S*)-AXT, *meso* AXT with either *S*- or *R*-end in the binding pocket.*

	Chemscore
(3*R*,3'*R*)-AXT	34,12
(3*S*,3'*S*)-AXT	34,73
meso AXT (*S*-end in the pocket)	36,10
meso AXT (*R*-end in the pocket)	33,59

*The highest binding affinity is found for the *meso* AXT with the *S*-end in the deep binding site region.